ORIGINAL ARTICLE

Synthesize, construction and enhanced performance of Bi$_2$WO$_6$/ZnS heterojunction under visible light: Experimental and DFT study

Liyun Yan [a,1], Jiahui Tang [a,1], Qing-an Qiao [a,*], Yunting Wang [a], Honglan Cai [a,*], Juan Jin [a,1], Hongwei Gao [b,*], Yanbin Xu [a]

[a] *School of Chemistry and Materials Science, Ludong University, Yantai 264025, PR China*
[b] *School of Life Science, Ludong University, Yantai 264025, PR China*

Abstract   With the simple perovskite structure, Bi$_2$WO$_6$ could be utilized as a modifier to overcome the low visible light response of the wide energy band photocatalyst ZnS. Flower-like Bi$_2$WO$_6$ was simply synthesized by hydrothermal method and Bi$_2$WO$_6$/ZnS heterojunction was constructed via solvothermal reaction. The results showed that ZnS nanospheres were uniformly loaded on the flower-like structure, which was well kept under low concentration loading ($\leq$20%ωt ZnS). The degradation of MB and Rh.B under visible light was used to measure the photocatalytic activity of the photocatalysts. The degradation rates of MB and Rh.B by 20%ωt-Bi$_2$WO$_6$/ZnS were as high as 94.3% and 92.8%, respectively. Moreover, the degradation performance of photocatalyst still maintained 89.3% after 4 times recycling tests. The visible light absorption ability of modified ZnS was improved, and the recombination of photogenerated electrons and holes was inhibited due to the formation of heterojunction. According to the data from density functional theory calculation, the composition of the valence band and conductive band of the Bi$_2$WO$_6$/ZnS system has been altered. The band gap of Bi$_2$WO$_6$/ZnS was reduced by roughly 1.12 eV compared to that of pure ZnS, and the work function analysis were in good agreement with the experimental results. Under light stimulation, electrons were transferred from Bi$_2$WO$_6$ to ZnS to produce superoxide radicals which played key roles in the degradation reaction of dyes.

* Corresponding authors.
  E-mail addresses: qiaoqa@sdu.edu.cn (Q.-a. Qiao), hognlancai74@ldu.edu.cn (H. Cai), gaohongw369@ldu.edu.cn (H. Gao).
[1] These authors contributed equally to this work.

1. Introduction

With the development of industrialization, synthetic dyes, various antibiotics and other organic synthetic substances were used in all aspects of human life. The organic dyes, which were highly toxic and difficult to degrade (Kusvuran et al., 2011; Routoula and Patwardhan, 2020), were discharged into natural systems such as water bodies, causing serious pollution to the environment and eventually threatening human's health (Yan et al., 2019). Traditional methods on treatment of organic dyes, including adsorption, electrochemical and biological methods (Yagub et al., 2014; Suhaimi et al., 2015; Paramaguru et al., 2010), had disadvantages such as incomplete degradation, secondary pollution, high energy consumption and poor stability (Ali, 2010; Lucas et al., 2008). Photocatalytic technology was a kind of light conversion technique, which converts the cleanest solar energy into chemical energy (Kudo and Miseki, 2009). Compared with the traditional treatment methods of organic waste, photocatalytic technology had the advantages of complete degradation, high efficiency and environmental protection (Kabra et al., 2004; Ismail and Bahnemann, 2014). The main advantage may be that it owns environmentally friendly characteristic.

ZnS had important applications in the field of photocatalysis because of its non-toxic, high electron mobility, low cost, high stability and rich nano-morpholog (Fang et al., 2011; Ashkarran, 2014; Bao et al., 2008). The main problem faced by ZnS as photocatalyst was the larger energy gap, which affected the efficiency of light absorption and utilization (Karan et al., 2010; Zhang et al., 2012; Wang et al., 2012). In order to get the desired results of photocatalysis, it is necessary to enhance the absorption ability of ZnS to visible light. Some semiconductors, such as Fe_2O_3 (Shah et al., 2015), ZnO (Zeng et al., 2021), CuO (Janani et al., 2022) and SnO_2 (Hu et al., 2016); were used to improve ZnS photocatalytic performance. In addition, studies on the recombination of two sulfide semiconductors, such as CdS/ZnS and CuS/ZnS, had also been reported (Fakhri and Ahmed, 2019; Zhang et al., 2011). The photocatalytic performance of ZnS has been improved by forming heterojunctions with specific semiconductors, which was proved to be a simple and efficient modification strategy from the previously researches.

Bismuth tungstate (Bi_2WO_6) was frequently explored in the field of photocatalysis because of its simple perovskite structure, narrow band gap and low cost (Chen et al., 2021; Orimolade et al., 2021; Longo et al., 2018). The valence band of Bi_2WO_6 was hybridized combination of Bi 6 s and O 2p orbitals (Meng and Zhang, 2016). As a result, the photocatalyst was allowed to be excited by visible light due to the reduction of energy gap. Bi_2WO_6 had simple preparation method and a diverse morphology (Liu et al., 2020; Zhang and Zhu, 2012), which could be used as an excellent modifier of ZnS. Tang et al. (Tang et al., 2015) prepared Bi_2WO_6/ZnS heterostructures by surface functionalization method with 3-mercaptopropionic acid (MPA) as surface functionalizer. The photodegradation efficiency of Rh.B by Bi_2WO_6/ZnS was about 1.85 times that of pure Bi_2WO_6. The enhanced photocatalytic activity of the synthetic heterostructures could be ascribed to the promotion of interfacial charge transfer and the inhibition of electron hole recombination, according to the characterization data. Safaei et al. (Safaei and Mohebbi, 2019) built Bi_2WO_6/ZnS hetero-nanostructures for aerobic selective alcohol oxidation by surface functionalization method with 4-mercaptosuccinic acid (MSA) at room temperature. The photooxidation yield of Bi_2WO_6/ZnS has enhanced as a consequence of the experiments. The charge recombination rate was reduced by the synergistic action of composites, resulting in effective charge separation of photogenerated electron-hole pairs. A Z-scheme-based ZnCdS/Bi_2WO_6 composite was fabricated by a three-step method (Zhao et al., 2021), which showed excellent stability and proved to be highly effective in the photodegradation of malachite green (MG) with enhanced photocatalytic activity under visible light. But the strategy was energy-consuming. From the previous studies (Chen et al., 2021; Orimolade et al., 2021; Liu et al., 2020), it can be found that there were a few reports on the research of Bi_2WO_6/ZnS heterojunction materials.

In this paper, flower-like Bi_2WO_6 was synthesized firstly by a simple hydrothermal method, and then the Bi_2WO_6/ZnS heterojunction was prepared by in-situ solvothermal method. The structure, morphology and optical properties of the prepared samples were analyzed by XRD, SEM, DRS and other characterization methods. The degradation of dyes under visible light was simulated to evaluate the photocatalytic performance of photocatalysts. The mechanism of photocatalysis was interpreted by means of both experiments and first-principle calculations. Our data showed that the Bi_2WO_6/ZnS heterojunction was a kind of stable photocatalyst with excellent performance and low energy cost.

2. Materials and methods

2.1. Chemicals

The chemicals, thiourea, $Bi(NO_3)_3·5H_2O$, $Na_2WO_4·2H_2O$ and $Zn(CH_3COO)_2·6H_2O$, were purchased from Aladdin Corp. Ethylene glycol and anhydrous ethanol were purchased from Sinopharm Chemical Reagent Ltd. Corp. The materials were analytical grade (99%) and used as received with no further purification. Deionized water was used in all experiments.

2.2. Synthesis of Bi_2WO_6 and Bi_2WO_6/ZnS photocatalyst

2.2.1. Synthesis of Bi_2WO_6 photocatalyst

Flower-like Bi_2WO_6 was prepared by hydrothermal method. In a typical procedure, 2.0 mmol of bismuth nitrate ($Bi(NO_3)_3·5H_2O$) was dissolved in 40 mL of deionized water, which was recorded as solution A. Similarly, 1.0 mmol of sodium tungstate ($Na_2WO_4·2H_2O$) was dissolved in 40 mL of deionized water, which was recorded as solution B. Then, solution B was added to the solution A, and a dropping process was carried out at about 2.0 mL•min^{-1}. The milky white precursor was obtained after the mixing and was transferred to a 100 mL teflon-lined autoclave and kept 6 h at 160 ℃. After cooling to room temperature, the product was washed three times with deionized water and anhydrous ethanol, respectively. The white solid product Bi_2WO_6 was obtained and dried in a vacuum drying oven at 60 ℃ for 10 h. The resulting white solid product Bi_2WO_6 was ground for subsequent use.

2.2.2. Synthesis of Bi_2WO_6/ZnS photocatalyst

In-situ solvothermal method was used for the synthesis of Bi_2WO_6/ZnS composite photocatalyst and the preparation process was shown in Fig. 1. Firstly, 0.3 g Bi_2WO_6 was ultrasonically dispersed in 40.0 mL ethylene glycol and $Zn(CH_3COO)_2·6H_2O$ was added to continue ultrasonication for 30 min(with different masses for each sample). The mixture was stirred for 30 min to make it disperse evenly. The resulting solution was recorded as solution C. Thiourea was weighed according to Zn: S molar ratio of 1:2.5, which proportion could eliminate ZnO component interference on ZnS nano microspheres (Wu et al., 2015). The weighed thiourea was stirred and dissolved in 40.0 mL of ethylene glycol, which recorded as solution D. A brownish yellow precursor was obtained after solution D was added slowly to solution C. The mixture solution was transferred to a 100 mL teflon-lined autoclave and heated to 180 ℃ and maintained at this temperature for 12 h. After cooling to room temperature, a
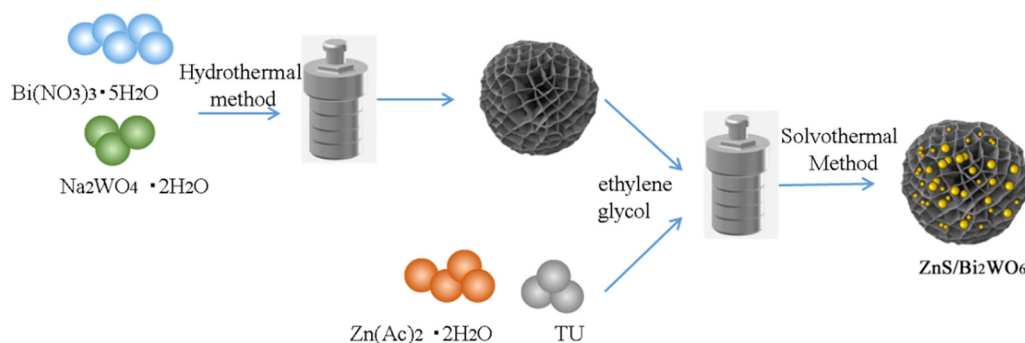
Fig. 1 Preparation of Bi$_2$WO$_6$/ZnS heterojunction.

brownish black precipitates were obtained by centrifugation. The precipitates were washed three times with deionized water and absolute ethanol. Finally, the composite Bi$_2$WO$_6$/ZnS photocatalyst was obtained by vacuum drying at 80 ℃ for 10 h. They were called Bi$_2$WO$_6$/ZnS-X (BWOZS-X), where X = 1–5, indicating the mass content of ZnS at 10%, 20%, 30%, 40% and 50% respectively. The corresponding mole ratios of Bi$_2$WO$_6$: ZnS were 1.258:1, 0.559:1, 0.326:1, 0.210:1 and 0.140:1. In addition, pure ZnS without Bi$_2$WO$_6$ was prepared under the same conditions.

2.3. Characterization

The phases of ZnS, Bi$_2$WO$_6$ and BWOZS were determined by X-ray diffraction (XRD, XD-3, China). The micro morphology of the photocatalyst was analysed by field emission scanning electron microscope (SEM, SU8010, Japan) at 200 kV. X-ray photoelectron spectroscopy (XPS, ESCALAB250, USA) of Thermo Electron Company of the United States was used to characterized the element composition and valence state of the sample. Al Kα was used as the excitation source and 12.5 kV was used as the working voltage. The specific surface area and pore size distribution analyzer (BET, ASAP2020, USA) of American micromeritics company was used to measure the adsorption isotherm of the sample with N$_2$ as the adsorption medium. The specific surface area, pore volume and pore size of the sample were calculated by Brunauer Emmet Teller (BET) formula and Barrett Joyner halenda (bjh) model. Before the test, the sample was degassed at 200 ℃ under vacuum for 12 h to remove the air and impurities adsorbed in the channel. The photoluminescence spectra (PL, HITACHI F-7100, Japan) were used to evaluate the carrier recom-bination. The spectral response range of photocatalyst was analysed by UV–Vis diffuse reflectance spectroscopy (DRS, Shimadzu SolidSpec-3700, Japan), and the wavelength range was from 240 nm to 800 nm. The energy gap (Eg) of ZnS, Bi$_2$WO$_6$ and BWOZS was determined from Tauc plot method (Soltani et al., 2012), which was a plot of $(\alpha h\upsilon)^2$ versus energy (hυ). Total organic carbon content analyzer (TOC, vario TOC, Germany) was used to characterize the total content of organic residue after photocatalytic process.

2.4. Photocatalysis evaluation

The photocatalytic performance was mainly confirmed by the removal of organic dyes under simulated visible light. Typically, 50 mL of MB or Rh. B solution (10 mg/L, pH = 7.5) was catalysed by 30 mg of photocatalyst at 20℃. A 300 W xenon arc lamp with the filter (< 420 nm) was used to simulate solar energy, and a mechanical stirrer with a stirring speed of 0–10000 rpm was used to stir the reaction solution. Before irradiation, the degradation system was stirred in the dark for 30 min to achieve adsorption–desorption equilibrium. During the test procedure, 2 mL of solution was taken out every 10 min to measure the concentration of MB or Rh.B. According to Lambert Beer's law (Yu et al., 2002), the concentration of the light-absorbing substances within a certain concentration range was directly proportional to the absorbance. Accordingly, the absorbance of MB and Rh. B solutions at 664 nm and 552 nm were recorded by UV–Vis spectrophotometer in the same way. The photocatalytic activity of photocatalyst was studied by analysing the degradation curves of organic dyes.

In order to explore the photocatalytic mechanism of heterojunction photocatalyst, isopropanol (IPA), benzoquinone (BQ) and disodium EDTA (EDTA-2Na) were used as scavengers for three active species: •OH, •O$_2^-$ and h$^+$ (Wu et al., 2019; Zhong et al., 2020). According to the ratio of n (scavenger): n $_{(dye)}$ = 10:1, the scavengers and 50 mL dyes were combined a 100 mL beaker. 30 mg photocatalyst was added to the above solution and the rest of the steps were the same as above.

2.5. The DFT calculations

The theoretical calculation was based on density functional theory (DFT) embedded in the CASTEP (Clark et al., 2005) software package. The generalized gradient approximation (GGA) with Perdew–Burke–Ernzerh (PBE) was used to describe the exchange correlation functional (Payne et al., 1992). The k-point meshes were set to 3 × 1 × 3 and 5 × 5 × 5 for structure optimization and electronic structure of ground-state Bi$_2$WO$_6$ and ZnS, respectively. The Hubbard U correction function was used to calculate the accurate energy gap of ZnS (Tang et al., 2013; Sharma et al., 2019) with the values of 4.8 eV for S 2p and 10.0 eV for Zn 3d (Khan et al., 2019) respectively. The band structure and density of states of Bi$_2$WO$_6$, ZnS and heterojunction were calculated by ultra-soft pseudopotential method (Monkhorst and Pack, 1976). The cut-off energy was set to 380 eV for ZnS, and 490 eV for Bi$_2$WO$_6$ and BWOZS (Liu et al., 2022; Pattnaik et al., 2018). In the process of structural optimization, the total

energy of the structure converged to 1×10^{-5} eV with the interatomic force and the maximum displacement to 0.03 eV/Å and 0.003 Å, respectively. In addition, the vacuum layer with a thickness of 20 Å was added to avoid the interference of periodic structure (Liu et al., 2021).

3. Results and discussion

3.1. Crystal structure and morphological analysis

The XRD spectra of the prepared samples were shown in Fig. 2. Pure zinc sulfide and pure Bi_2WO_6 can be easily distinguished into hexagonal system and triclinic system by comparison with standard PDF (JCPDS card No. 99-0097 and JCPDS card No. 79-2381). The spectral peak of pure Bi_2WO_6 appeared at $2\theta = 28.2°$, 32.6°, 47.0°, 55.7°, 58.5°, 68.5°, 75.8° and 78.2°. These peaks were resolved into (131), (200), (202), (133), (262), (400), (103) and (204) crystal planes, respectively. It was proved that the orthogonal phase Bi_2WO_6 was successfully synthesized. The spectrums of the BWOZS-X photocatalysts were similar to that of pure Bi_2WO_6. The peak intensity decreased gradually with the increase of ZnS content, but no obvious ZnS peak was found. The characteristic peak of ZnS was not detected (Mosleh et al., 2019), which may be caused by the fact that ZnS had a high dispersion owing to flower-like structure of Bi_2WO_6 (Chen et al., 2021). On the other hand, the solvothermal method with ethylene glycol solvent could lead to a low crystallinity of tiny ZnS particles difficult to be identified by XRD (Wang et al., 2022; Bashar et al., 2020).

3.2. Morphology and microstructure

The morphology of the sample was characterized by SEM, and the results were shown in Fig. 3.The flower-like Bi_2WO_6 was self-assembled from a large number of Bi_2WO_6 nano sheets (Fig. 3 a). This structure was used as the substrate for the growth of ZnS to inhibit the agglomeration. The rich pores among the sheets could be helpful to the better adsorption of dyes in photocatalytic process. The SEM of BWOZS-1 was shown in Fig. 3 (b,c). ZnS nanospheres with a size of about

50–100 nm were evenly dispersed on the flower pieces of Bi_2WO_6.

The observation of BWOZS-2 was similar to that of BWOZS-1, which confirms the successful combination of the Bi_2WO_6 and the ZnS. However, the flower-like structure of Bi_2WO_6 was destroyed with the increasing content of ZnS in Fig. 3(f-h). The distribution of ZnS nanospheres on the surface of Bi_2WO_6 gradually increased, and the flower-like structure of Bi_2WO_6 was destroyed due to ZnS agglomeration. ZnS nanospheres and Bi_2WO_6 nanosheets were agglomerated with each other, which is not conducive to the improvement of photocatalytic performance. Therefore, a low content loading of ZnS was considered beneficial to keep the flower-like structure of Bi_2WO_6.

3.3. XPS analysis

X-ray photoelectron spectroscopy (XPS) was used to study the chemical composition and environment of elements in BWOZS-2 to determine the composite state of the composites. The XPS results of BWOZS-2 were shown in Fig. 4. The constituent elements of the composite, including Bi, W, O, Zn and S, could be found corresponding peaks in Fig. 4 (a) to prove the successful preparation of BWOZS. There were two peaks at 1023.3 eV and 1046.3 eV in the high-resolution XPS spectra of Zn 2p in Fig. 4 (b), which correspond to the binding energy of Zn $2p_{3/2}$ and Zn $2p_{1/2}$, respectively (Fang et al., 2015). It was proved that Zn existed in the form of Zn^{2+}. In Fig. 5(c), the pronounced XPS spectrum for O 1 s was deconvoluted into two peaks at 530.6 eV and 531.4 eV, which were assigned to the lattice oxygen component in $[Bi_2O_2]^{2+}$, $[WO_4]^{2-}$ and OH hydroxyl groups (Zhang et al., 2011). The characteristic peaks of tungsten 4f at 35.2 eV and 37.2 eV shown in Fig. 4 (d) were corresponded to the binding energy of $4f_{7/2}$ and W $4f_{5/2}$ respectively, indicating that tungsten existed in the form of W^{6+} in the heterojunction (Lu et al., 2017). The XPS spectrum of Bi 4f in Fig. 4 (e) exhibited two peaks at 158.9 eV and 164.2 eV due to the binding energy of Bi $4f_{7/2}$ and Bi $4f_{5/2}$, which proved that bismuth element exists in the form of Bi^{3+} in the lattice of Bi2WO6 (Fu et al., 2013). The two peaks at 161.3 eV and 162.9 eV in Fig. 5(f) were assigned to S $2p_{3/2}$ and S $2p_{1/2}$, respectively (Jiang et al., 2016).

3.4. BET analysis

The adsorption performance of photocatalyst was investigated by specific surface area (Table 1) and pore size analysis technology (Fig. 5). The optimum specific surface area (S_{BET}) of ZnS nanospheres was 90.42 $m^2 \cdot g^{-1}$, which was much higher than 18.82 $m^2 \cdot g^{-1}$ of micron-flower-like Bi_2WO_6. When the heterojunction was created following ZnS deposition, the S_{BET} gradually increased with the increase of ZnS concentration. Fig. 5 showed the N_2 isothermal adsorption desorption curves of ZnS, Bi_2WO_6 and BWOZS-2. The curves of the ZnS, Bi_2WO_6 and BWOZS-2 were class IV curves by BDDT classification method and had hysteresis rings representing mesoporous structure. Therefore, the mesoporous structures of ZnS, Bi_2WO_6 and BWOZS-2 were confirmed. For the heterojunctions, both the pore volume and pore diameter were decreasing with the incressing content of ZnS. Light scattering was better utilized for materials with larger pore volume and larger pore size
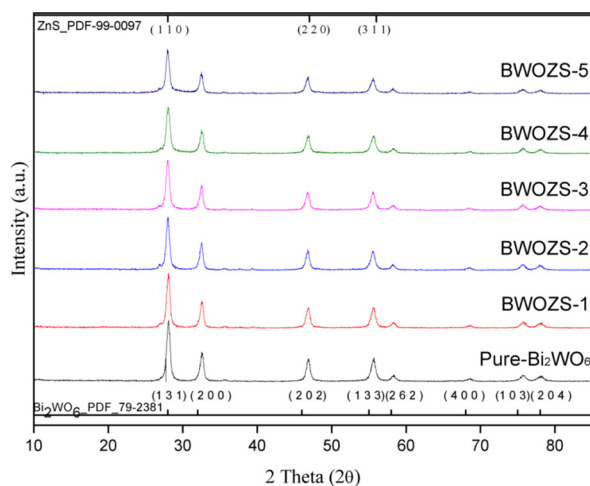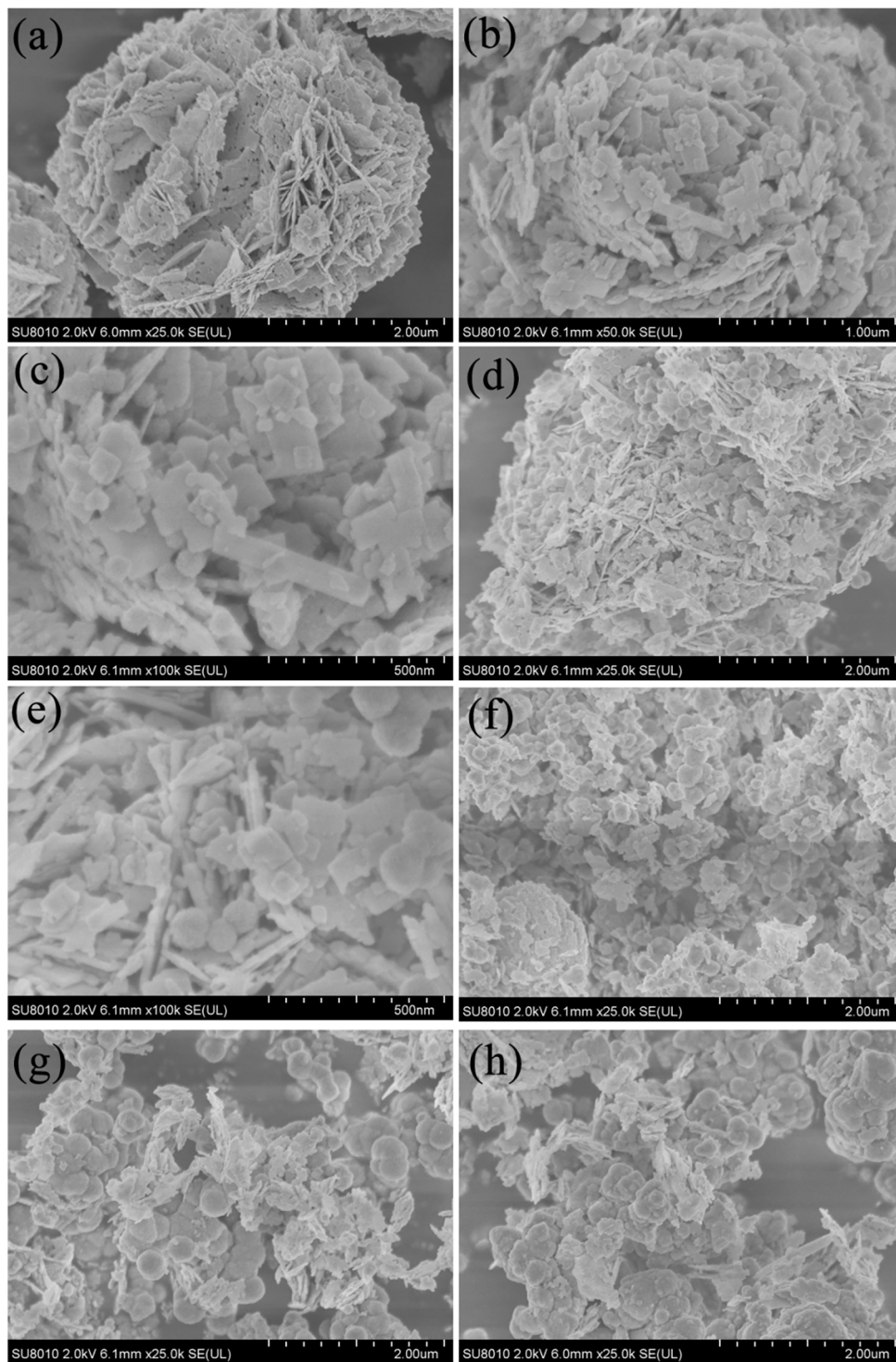

**Fig. 2** XRD spectra of the prepared samples.

Fig. 3 SEM image of prepared samples. (a: pure-Bi$_2$WO$_6$, b-c: BWOZS-1, d-e:BWOZS-2, f: BWOZS-3, g: BWOZS-4, h: BWOZS-5).

(Wu et al., 2008), in which the photocatalytic activity was significantly improved. The high concentration of ZnS loading could destroy some of the pore structure of Bi$_2$WO$_6$. As a result, a relatively low content of ZnS would be preferred to the improvement of photocatalytic performance for the heterojunctions.

3.5. PL and UV–vis DRS analysis

The carrier recombination of photocatalyst was investigated and characterized by PL, which the results were shown in Fig. 6. The obvious wide emission peak at 430–480 nm belonged to the intrinsic luminescence of Bi$_2$WO$_6$, which orig-
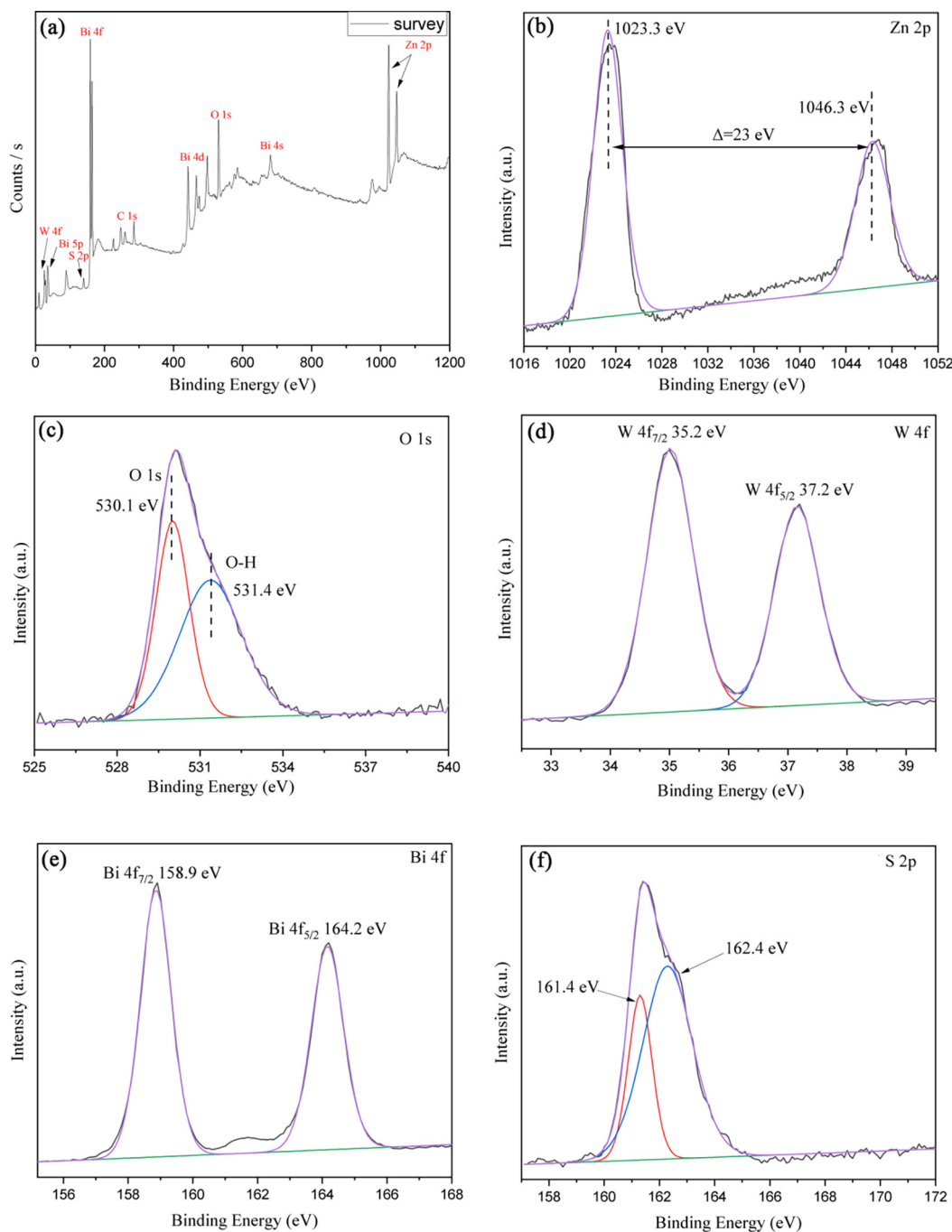
Fig. 4   XPS spectrum of BWOZS-2.

inated from the photogenerated electron transfer transition from the hybrid valence band of Bi 6 s and O 2p to the empty conduction band of W 5d orbit in WO_4^{2-} (Wang et al., 2014). The fluorescence emission peak intensity of heterojunction decreased obviously after ZnS was added, which proved that the recombination rate of photogenerated electron and hole pair was low under light irradiation (Fu et al., 2013). The heterojunction emission intensity in low concentration ZnS (≤20%ωt) compositing was substantially lower than that in high concentration (≥30%ωt). Based on the results of SEM, it can be revealed that the increasing concentration of ZnS led to the high aggregation of the heterojunction.

The spectral response range of photocatalyst was investigated through UV–vis DRS, and the results were shown in Fig. 7. Pure ZnS had little response to visible light, and the absorption band edge was about 400 nm. When Bi_2WO_6 and ZnS were combined to create the heterojunction, the visible light absorption intensity of BWOZS-X was much greater than that of ZnS, which was attributable to the introduction of Bi_2WO_6 with small band gap. The band gap energies of the five samples of BWOZS-X heterojunctions were determined in Fig. 7b, which were 3.18 eV, 3.12 eV, 3.27 eV, 3.48 eV and 3.56 eV, respectively. One can find that ZnS absorbs more light from 300 to 400 nm while Bi_2WO_6 has a higher absorbance
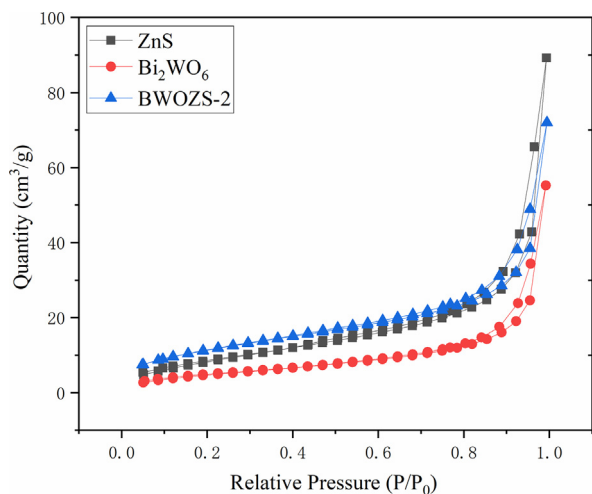
Fig. 5 N$_2$ isothermal adsorption desorption curves of ZnS, Bi$_2$WO$_6$ and BWOZS-2.

Table 1 Specific surface area and pore size analysis of ZnS, Bi$_2$WO$_6$ and BWOZS-X(X = 1-3).

sample	S$_{BET}$ (m^2/g)	BJH pore volume (cm^3/g)	BJH pore Width (nm)
ZnS	90.42	0.0421	4.376
Bi$_2$WO$_6$	18.82	0.0861	16.940
BWOZS-1	33.73	0.1381	15.659
BWOZS-2	42.52	0.1106	10.802
BWOZS-3	51.29	0.0841	9.497
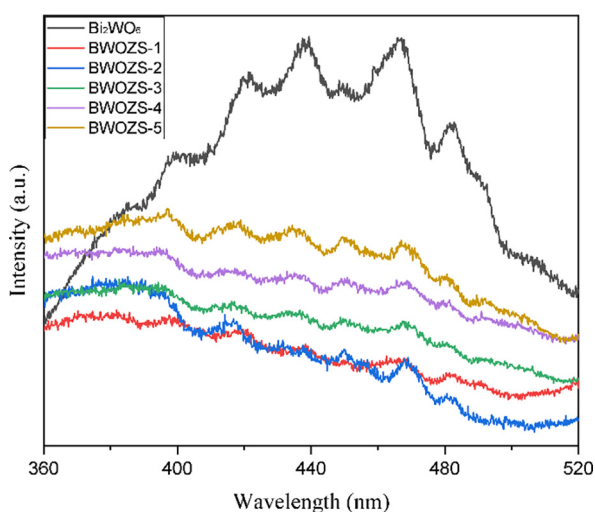
Fig. 6 PL spectra of the prepared samples.

from 450 to 800 nm (Gao et al., 2020). BWOZS-2 had the smallest energy gap (3.12 eV) among all of them and exhibited a progressive redshift with the absorbance edge about 570 nm (Tang et al., 2015). It demonstrated that the heterostructure

formed at the mole ratio of 0.559:1 (Bi$_2$WO$_6$: ZnS) was the most appropriate one and had the best visible light response.

3.6. Photocatalytic performance and mechanism

In order to evaluate the photocatalytic performance of the prepared samples, the typical dyes, Methylene Blue (MB) and Rhodamine B (Rh.B), were degraded under simulated visible light and the results were shown in Fig. 8. Pure ZnS and Bi$_2$WO$_6$ had worsedegradation effect on MB(37.9% and 39.9%, respectively). In contrast, the degradation rate of MB by heterojunction was significantly higher than that of pure ZnS and Bi$_2$WO$_6$. The results of Rh.b degradation by heterojunction in Fig. 8 (b) were similar with those of MB. Visible light was effectively utilized and photogenerated electrons and holes were effectively separated due to the formation of heterostructures, which played a key role in the improvement of photocatalytic performance. Furthermore, the photocatalytic performance of heterojunctions increased initially and subsequently declined as the ZnS concentration increased, indicating that the composite structure of BWOZS-X had a substantial impact on photocatalysis. Obviously, the 20%ωt composite sample (BWOZS-2) showed the best degradation effect on MB and Rh.B with 94.3% and 92.8% degradation rate. This was consistent with the above analysis of the characterization results. Compared with previous study (Tang et al., 2015), the energy gap of BWOZS-2 was 3.12 eV which was slightly higher than the reported value 2.86 eV, but the photocatalytic activity for Rh.B degradation (92.8%) was higher than the reported value of 87.1%.

The stability of photocatalyst was also investigated by simulated cyclic degradation of MB. The results of the BWOZS-2 recycling test were shown in Fig. 9(a). The degradation rate decreases from 94.3% to 92.1% and finally stabilized at about 89.3% after four cycles. The performance of the photocatalyst decreased at about 5%, which may be related to the occupation of active sites of BWOZS-2 (Peng et al., 2019).

After photocatalysis, total organic carbon (TOC) analysis was performed(Fig. 9(b)) on the residue to assess if the MB was totally mineralized (Beltrán et al., 2010). The total organic carbon content of MB was used as the standard (100%), which was the base to achieve the TOC results of pure ZnS and BWOZS-2. The disparity between BWOZS-2 and pure ZnS was remarkably via the observation. The rate of mineralization of ZnS was only 13.7%, which was similar to the rate of photocatalytic MB degradation. The mineralization rate of the BWOZS-2 heterostructure was 84.33 %, which was about 5.7 times greater than that of pure ZnS. However, a limited number of MB still unmineralized in BWOZS-2 due to the fact that the small organic fragment from the breakdown of the carbon nitrogen heterocycle structure in MB had no further degradation (Houas et al., 2001). BWOZS-2 heterojunction was proved to have good photocatalytic performance by TOC.

The active substance capture experiment was meant to determine the important active chemicals in the photocatalytic process. The capture experimental results were shown in Fig. 10. The deterioration rate of the experimental group utilizing *p*-benzoquinone (BQ) reduced greatly, followed by isopropyl alcohol (IPA), while EDTA-2Na had the least influence to the degradation of Rh.B. As a result, it was reasonable to believe that •O$_2^-$ played the most role in the reac-
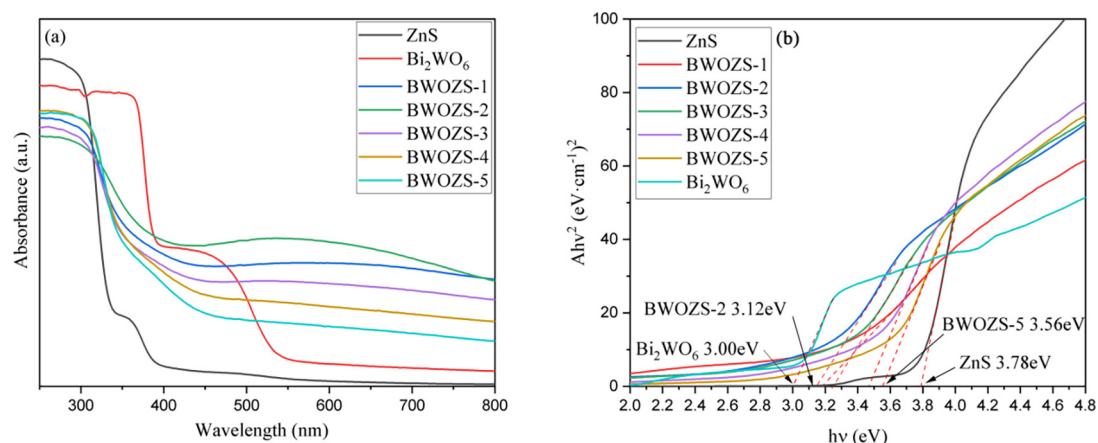
Fig. 7 DRS spectra of the prepared samples (a) and Tauc plot of $(\alpha h\nu)^2$ versus photon energy (hν) (b).
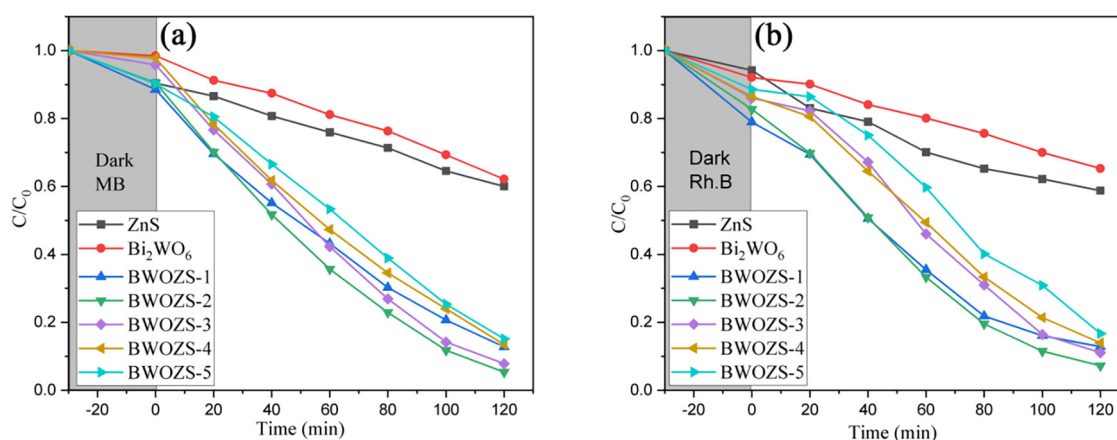

Fig. 8 Photocatalytic degradation of dye MB(a), Rh.B (b)of prepared samples.
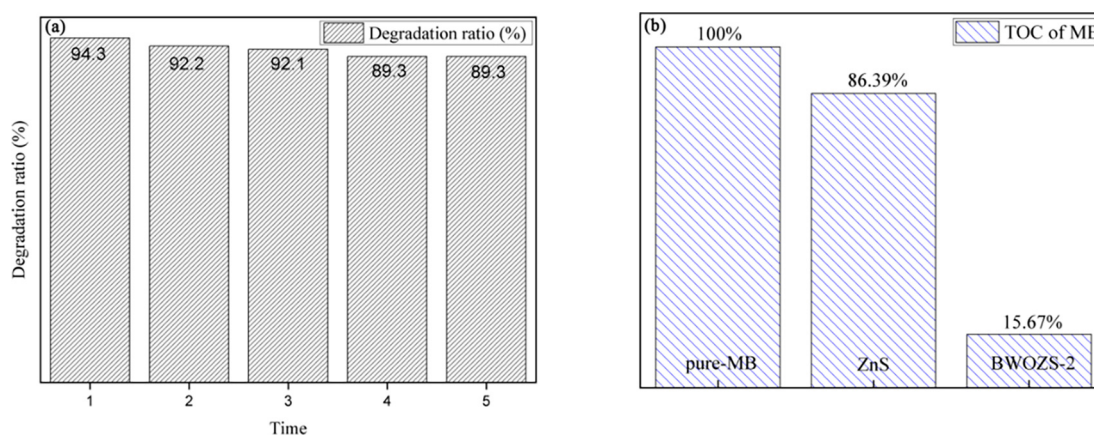

Fig. 9 Recycling test of MB degradation by BWOZS-2 under visible light (a), and the results of TOC (b).

tion. In addition, •OH and the hole had been taken parts in the degradation. The cases for MB were similar to those of Rh.B.

The photocatalytic mechanism of Bi_2WO_6/ZnS was illustrated in Fig. 11. When Bi_2WO_6/ZnS was stimulated by the visible light, the electrons and holes of Bi_2WO_6 would be transferred to conduction band minimum (CBM) and valence band

maximum (VBM) of Bi_2WO_6, respectively. Due to the position shift of the heterojunction band structure, the electrons migrated further to the CBM of ZnS, where the electrons reacted with the dissolved oxygen to form $\bullet O_2^-$. At the same time, the migration of holes from ZnS VBM to Bi_2WO_6 VBM created an effective internal electric field, which acceler-
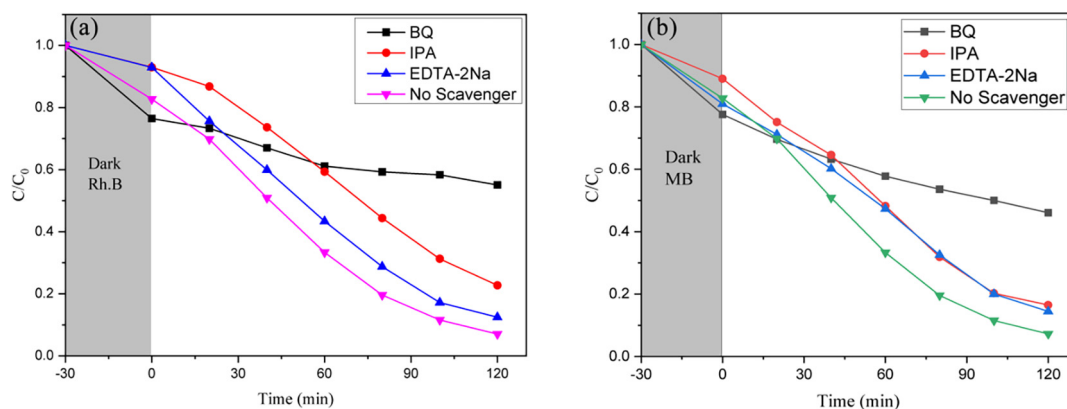
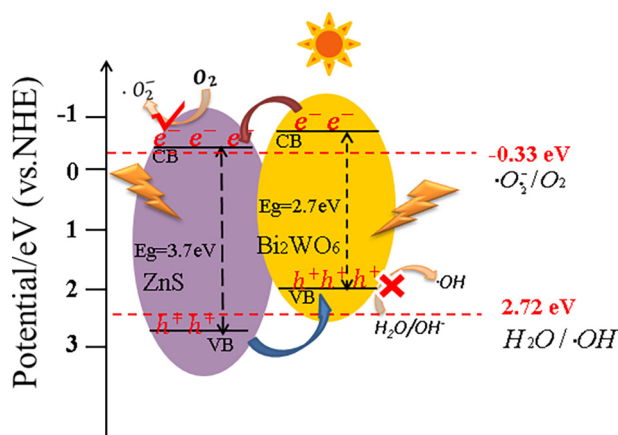**Fig. 10** Active species capture experiment Rh.B(a) and MB (b).

Fig. 11 Photocatalytic reaction mechanism of BWOZS.

ated the transfer and separation of electron hole pairs. It was worth noting that $\bullet O_2^-$ could be generated because the redox potential of CBM (ZnS) was more negative than -0.33 eV ($\bullet O_2^-/O_2$). However, the potential of VBM (Bi_2WO_6) was not enough to produce $\bullet OH$. Finally, the dye was oxidized and decomposed into small carbon chains by $\bullet O_2^-$ and h^+, and most of them were mineralized into CO_2 and H_2O.

3.7. DFT calculations

ZnS (110) and Bi_2WO_6 (100) planes were used to construct the heterostructure model of BWOZS according to the above XRD results (supporting information Fig. 1). The energy gap of pure ZnS, Bi_2WO_6 and heterojunction BWOZS were 3.653 eV, 2.201 eV and 2.537 eV respectively(supporting information Fig. 2), which were close to the report values (Hoa et al., 2009; Liao et al., 2011). Compared to pure ZnS, the band gap width of BWOZS was reduced by 1.12 eV. The deference between the theoretical value and experimental results probably came from the fact that theoretical calculations were carried out in a vacuum environment.

The analysis of the density of states (DOS) and projected density of states (PDOS) was very useful to investigate the electronic structure of heterojunctions. The DOS (supporting information Fig. 2) showed that the VB of pure ZnS was composed of p and d orbitals and the CB was composed of s and p

orbitals. Specifically, the deep level of the valence band was contributed by the Zn 3d orbital, and the edge of the valence band was occupied by the S 2p orbital. The edge of the conduction band was mainly composed of Zn 4 s and 3p orbitals. The energy gap reduced by 1.116 eV after Bi_2WO_6 added to form the heterojunction. Furthermore, the generation of the heterojunction relieved the Zn 3d electron bound state at the deep level of VB by moving it to the shallow level, which was more conducive to the carrier migration in the semiconductor (Akhtar et al., 2015). Compared with pure ZnS, the VB of BWOZS had a greater electronic state density after the introduction of Bi_2WO_6, which may be related to the electron transfer of Bi_2WO_6 to ZnS. The main contributions of CBM of BWOZS heterojunction were W 5d, Bi 6p and O 2p orbits, and the contributions of VBM were S 2p, Bi 6 s, and O 2p orbits (supporting information Fig. 2). The above results showed that the electrons of Bi_2WO_6 and ZnS were staggered in different CB and VB regions, which was very similar to type-II heterojunction (Nayfeh et al., 2008). The addition of Bi_2WO_6 was critical for properly separating the photogenerated carriers at the interface and increasing photocatalytic activity.

The optical characteristics simulation results were shown in supporting information Fig. 3. The distinctive absorption of ZnS in UV-region was its greatest absorption peak. The absorption wavelength edge of pure ZnS was around 420 nm, which was consistent with the experimental result. On the other hand, the UV absorption of BWOZS was greatly reduced, and the absorption wavelength edge extended to roughly 600 nm. The simulation results revealed that the addition of Bi_2WO_6 improved the responding range of ZnS to visible light, which was in line with above experimental results of DRS.

In order to explain the migration mechanism of electrons and holes, the work function of the photocatalysts was calculated as well (Fig. 12). The value for the work functions of ZnS, Bi_2WO_6 and BWOZS were 7.549 eV, 6.289 eV and 7.045 eV, respectively. The work function of Bi_2WO_6 was lower than that of ZnS. As a result, the photogenerated electrons flowed from Bi_2WO_6 to ZnS and the holes moved in the opposite direction when the BWOZS heterojunction was irradiated by visible light. At last, the Fermi level of them was came to equal. The internal electric field created by electron and hole migration could accelerate the separation of them more effectively. Consequently, the electrons were con-
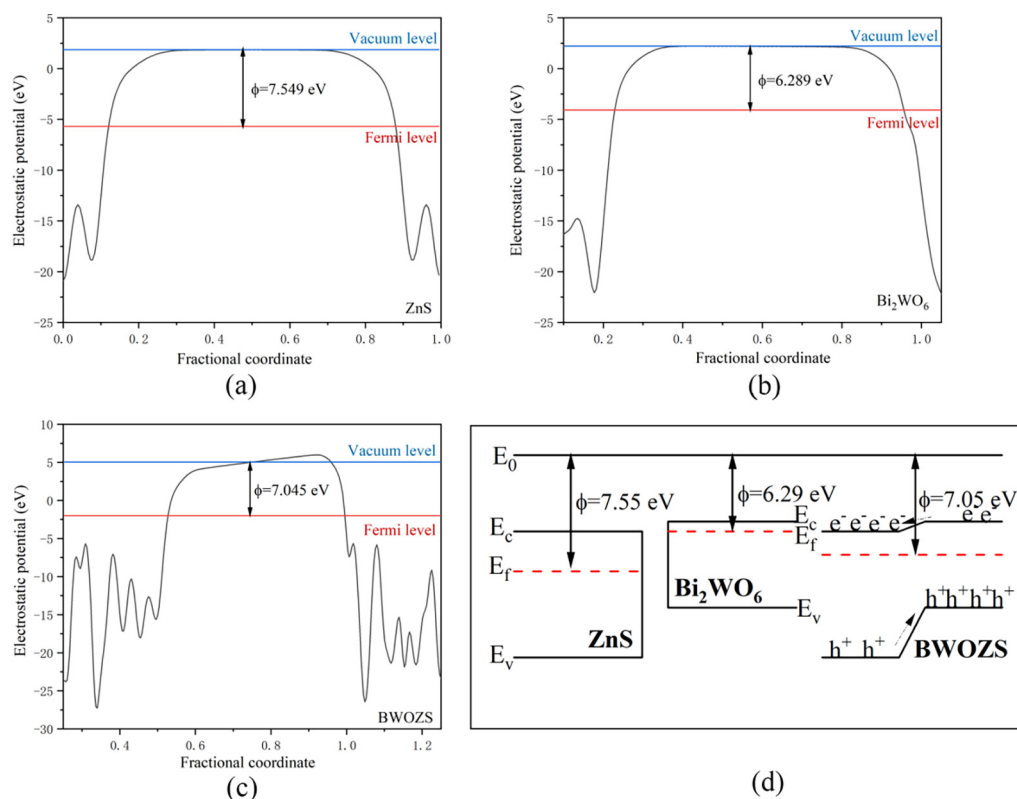
Fig. 12 Work functions of ZnS (a), Bi_2WO_6 (b) and BWOZS (c).

gregated in the CBM of ZnS while holes were congregated in the VBM of Bi_2WO_6. The energy gap of the heterojunction was narrowed, which made it much easier to be activated by visible light.

4. Conclusions

In conclusion, the flower-like Bi_2WO_6 was synthesized by hydrothermal method, and the Bi_2WO_6/ZnS heterojunction was constructed by in-situ solvothermal method. ZnS nanospheres were uniformly loaded with flower-like structures which were not damaged under low concentration loading ($\leq$20%ωt). The 20%ωt-Bi_2WO_6/ZnS heterojunction had a relatively large specific surface area of 42.52 m^2/g, which was the most favorable product among all the samples in PL and DRS characterization. The photocatalytic activity of Bi_2WO_6/ZnS heterojunction was investigated with the degradation of MB and Rh.B under visible light. Compared with pure ZnS and Bi_2WO_6, the photocatalytic performance of 20%ωt-Bi_2WO_6/ZnS photocatalyst was significantly improved. The degradation rates of MB and Rh.B by 20%ωt-Bi_2WO_6/ZnS were as high as 94.3% and 92.8%, respectively. Moreover, the degradation performance of photocatalyst still maintained 89.3% after 4 times recycling tests indicating its excellent stability. The energy gap was decreased because of the addition of Bi_2WO_6, and the absorption edge of Bi_2WO_6/ZnS was extended to the visible range at about 600 nm. The photocatalytic mechanism was explained both from experiments and DFT calculations. Under light stimulation, the electrons transferred from Bi_2WO_6 to ZnS and further produced superoxide radical, which participated in the dye degradation reaction. What' more, the results from DFT calculation indicated that the photogenerated electrons flowed from Bi_2WO_6 to ZnS and the holes moved in the opposite direction when the BWOZS heterojunction was irradiated by visible light. The narrower

energy gap of the heterojunction would make it much easier to be activated by visible light. These results will be valuable for the further researches in this field.

Declaration of Competing Interest

The authors declare that they have no known competing financial interests or personal relationships that could have appeared to influence the work reported in this paper.

Appendix A. Supplementary material

Supplementary data to this article can be found online at https://doi.org/10.1016/j.arabjc.2023.104760.

References

Akhtar, M.S., Malik, M.A., Riaz, S., Naseem, S., 2015. Room temperature ferromagnetism and half metallicity in nickel doped ZnS: experimental and DFT studies. Mater. Chem. Phys. 160, 440–446.

Ali, H., 2010. Biodegradation of synthetic dyes—a review. Water Air Soil Pollut. 213 (1), 251–273.

Ashkarran, A.A., 2014. Absence of photocatalytic activity in the presence of the photoluminescence property of Mn–ZnS nanoparticles prepared by a facile wet chemical method at room temperature. Mater. Sci. Semicond. Process. 17, 1–6.

Bao, N., Shen, L., Takata, T., Domen, K., 2008. Self-templated synthesis of nanoporous CdS nanostructures for highly efficient photocatalytic hydrogen production under visible light. Chem. Mater. 20 (1), 110–117.

Bashar, M.S., Matin, R., Sultana, M., Siddika, A., Rahaman, M., Gafur, M.A., Ahmed, F., 2020. Effect of rapid thermal annealing on structural and optical properties of ZnS thin films fabricated by RF magnetron sputtering technique. J. Theor. Appl. Phys. 14 (1), 53–63.

Beltrán, F.J., Aguinaco, A., García-Araya, J.F., 2010. Kinetic modelling of TOC removal in the photocatalytic ozonation of diclofenac aqueous solutions. Appl. Catal. B: Environ. 100 (1–2), 289–298.

Chen, T., Liu, L., Hu, C., Huang, H., 2021. Recent advances on Bi$_2$WO$_6$-based photocatalysts for environmental and energy applications. Chin. J. Catal. 42 (9), 1413–1438.

Clark, S.J., Segall, M.D., Pickard, C.J., Hasnip, P.J., Probert, M.I., Refson, K., Payne, M.C., 2005. First principles methods using CASTEP. Zeitschrift für Kristallogr.-Crystall. Mater. 220 (5–6), 567–570.

Fakhri, F.H., Ahmed, L.M., 2019. Incorporation CdS with ZnS as composite and using in photo-decolorization of congo red dye. Indonesian J. Chem. 19 (4), 936–943.

Fang, Z., Weng, S., Ye, X., Feng, W., Zheng, Z., Lu, M., Lin, S., Fu, X., Liu, P., 2015. Defect engineering and phase junction architecture of wide-bandgap ZnS for conflicting visible light activity in photocatalytic H$_2$ evolution. ACS Appl. Mater. Interfaces 7 (25), 13915–13924.

Fang, X., Zhai, T., Gautam, U.K., Li, L., Wu, L., Bando, Y., Golberg, D., 2011. ZnS nanostructures: from synthesis to applications. Prog. Mater. Sci. 56 (2), 175–287.

Fu, Y., Chang, C., Chen, P., Chu, X., Zhu, L., 2013. Enhanced photocatalytic performance of boron doped Bi$_2$WO$_6$ nanosheets under simulated solar light irradiation. J. Hazard. Mater. 254, 185–192.

Gao, Y., Liu, S., Wang, Y., Zhao, P., Li, K., He, J., Liu, S., 2020. Fabrication of nitrogen defect mediated direct Z scheme g-C$_3$N$_x$/Bi$_2$WO$_6$ hybrid with enhanced photocatalytic properties. J. Colloid Interface Sci. 579, 177–185.

Hoa, T.T.Q., Wu, L.V., Canh, T.D., Long, N.N. In *Preparation of ZnS nanoparticles by hydrothermal method*, Journal of Physics: Conference Series, IOP Publishing: 2009; p 012081.

Houas, A., Lachheb, H., Ksibi, M., Elaloui, E., Guillard, C., Herrmann, J.-M., 2001. Photocatalytic degradation pathway of methylene blue in water. Appl. Catal. B: Environ. 31 (2), 145–157.

Hu, L., Chen, F., Hu, P., Zou, L., Hu, X., 2016. Hydrothermal synthesis of SnO$_2$/ZnS nanocomposite as a photocatalyst for degradation of Rhodamine B under simulated and natural sunlight. J. Mol. Catal. A Chem. 411, 203–213.

Ismail, A.A., Bahnemann, D.W., 2014. Photochemical splitting of water for hydrogen production by photocatalysis: a review. Sol. Energy Mater. Sol. Cells 128, 85–101.

Janani, B., Okla, M.K., Abdel-Maksoud, M.A., AbdElgawad, H., Thomas, A.M., Raju, L.L., Al-Qahtani, W.H., Khan, S.S., 2022. CuO loaded ZnS nanoflower entrapped on PVA-chitosan matrix for boosted visible light photocatalysis for tetracycline degradation and anti-bacterial application. J. Environ. Manage. 306, 114396.

Jiang, D., Sun, Z., Jia, H., Lu, D., Du, P., 2016. A cocatalyst-free CdS nanorod/ZnS nanoparticle composite for high-performance visible-light-driven hydrogen production from water. J. Mater. Chem. A 4 (2), 675–683.

Kabra, K., Chaudhary, R., Sawhney, R.L., 2004. Treatment of hazardous organic and inorganic compounds through aqueous-phase photocatalysis: a review. Ind. Eng. Chem. Res. 43 (24), 7683–7696.

Karan, N.S., Sarma, D., Kadam, R., Pradhan, N., 2010. Doping transition metal (Mn or Cu) ions in semiconductor nanocrystals. J. Phys. Chem. Lett. 1 (19), 2863–2866.

Khan, M.S., Shi, L., Yang, X., Ali, S., Ullah, H., Zou, B., 2019. Optoelectronic and magnetic properties of Mn-doped and Mn–C co-doped Wurtzite ZnS: a first-principles study. J. Phys. Condens. Matter 31, (39) 395702.

Kudo, A., Miseki, Y., 2009. Heterogeneous photocatalyst materials for water splitting. Chem. Soc. Rev. 38 (1), 253–278.

Kusvuran, E., Gulnaz, O., Samil, A., Yildirim, Ö., 2011. Decolorization of malachite green, decolorization kinetics and stoichiometry of ozone-malachite green and removal of antibacterial activity with ozonation processes. J. Hazard. Mater. 186 (1), 133–143.

Liao, Y.-H.-B., Wang, J.X., Lin, J.-S., Chung, W.-H., Lin, W.-Y., Chen, C.-C., 2011. Synthesis, photocatalytic activities and degradation mechanism of Bi$_2$WO$_6$ toward crystal violet dye. Catal. Today 174 (1), 148–159.

Liu, X., Gu, S., Zhao, Y., Zhou, G., Li, W., 2020. BiVO$_4$, Bi$_2$WO$_6$ and Bi$_2$MoO$_6$ photocatalysis: a brief review. J. Mater. Sci. Technol. 56, 45–68.

Liu, T., Li, H., Gao, J., Ding, S., Liu, X., Jia, H., Xue, J., 2022. Effect of oxygen vacancies on the photocatalytic CO$_2$ reduction performance of Bi$_2$WO$_6$: DFT and experimental studies. Appl. Surf. Sci. 579, 152135.

Liu, J., Wang, T., Nie, Q., Hu, L., Cui, Y., Tan, Z., Yu, H., 2021. One-step synthesis of metallic Bi deposited Bi$_2$WO$_6$ nanoclusters for enhanced photocatalytic performance: an experimental and DFT study. Appl. Surf. Sci. 559, 149970.

Longo, C., Galante, M.T., Fitzmorris, R., Zhang, J.Z., Taylor, S.F.R., Mohapatra, J., Liu, J.P., Duarte, L.G.T.A., Hossain, M.K., Hardacre, C., Rajeshwar, K., 2018. Complex oxides based on silver, bismuth, and tungsten: syntheses, characterization, and photoelectrochemical behavior. J. Phys. Chem. C 122 (25), 13473–13480.

Lu, J., Wang, Y., Liu, F., Zhang, L., Chai, S., 2017. Fabrication of a direct Z-scheme type WO$_3$/Ag$_3$PO$_4$ composite photocatalyst with enhanced visible-light photocatalytic performances. Appl. Surf. Sci. 393, 180–190.

Lucas, N., Bienaime, C., Belloy, C., Queneudec, M., Silvestre, F., Nava-Saucedo, J.-E., 2008. Polymer biodegradation: mechanisms and estimation techniques–a review. Chemosphere 73 (4), 429–442.

Meng, X., Zhang, Z., 2016. Bismuth-based photocatalytic semiconductors: introduction, challenges and possible approaches. J. Mol. Catal. A Chem. 423, 533–549.

Monkhorst, H.J., Pack, J.D., 1976. Special points for Brillouin-zone integrations. Phys. Rev. B 13 (12), 5188.

Mosleh, S., Dashtian, K., Ghaedi, M., Amiri, M., 2019. A Bi$_2$WO$_6$/Ag$_2$S/ZnS Z-scheme heterojunction photocatalyst with enhanced visible-light photoactivity towards the degradation of multiple dye pollutants. RSC Adv. 9 (52), 30100–30111.

Nayfeh, O.M., Chleirigh, C.N., Hennessy, J., Gomez, L., Hoyt, J.L., Antoniadis, D.A., 2008. Design of tunneling field-effect transistors using strained-silicon/strained-germanium type-II staggered heterojunctions. IEEE Electron Device Lett. 29 (9), 1074–1077.

Orimolade, B.O., Idris, A.O., Feleni, U., Mamba, B., 2021. Recent advances in degradation of pharmaceuticals using Bi$_2$WO$_6$ mediated photocatalysis–a comprehensive review. Environ. Pollut. 289, 117891.

Paramaguru, G., Kathiravan, A., Selvaraj, S., Venuvanalingam, P., Renganathan, R., 2010. Interaction of anthraquinone dyes with lysozyme: evidences from spectroscopic and docking studies. J. Hazard. Mater. 175 (1–3), 985–991.

Pattnaik, A.; Tomar, M.; Jha, P. K.; Bhoi, A. K.; Gupta, V.; Prasad, B., Theoretical analysis of the electrical and optical properties of ZnS. In *Advances in Systems, Control and Automation*, Springer: 2018; pp 9-19

Payne, M.C., Teter, M.P., Allan, D.C., Arias, T.A., Joannopoulos, J. D., 1992. Iterative minimization techniques for ab initio total-

energy calculations: molecular dynamics and conjugate gradients. Rev. modern phys. 64 (4), 1045.

Peng, H., Liu, D., Zheng, X., Fu, X., 2019. N-doped carbon-coated ZnS with sulfur-vacancy defect for enhanced photocatalytic activity in the visible light region. Nanomaterials 9 (12), 1657.

Routoula, E., Patwardhan, S.V., 2020. Degradation of anthraquinone dyes from effluents: a review focusing on enzymatic dye degradation with industrial potential. Environ. Sci. Tech. 54 (2), 647–664.

Safaei, E., Mohebbi, S., 2019. Boosted photocatalytic performance of uniform hetero-nanostructures of Bi_2WO_6/CdS and Bi_2WO_6/ZnS for aerobic selective alcohol oxidation. J. Photochem. Photobiol. A Chem. 371, 173–181.

Shah, P., Siddhapara, K., Shah, D., 2015. Structural, optical, and photocatalytic properties of $ZnS/\alpha\text{-}Fe_2O_3$ core shell nano particles. Russ. J. Gen. Chem. 85 (3), 689–691.

Sharma, M., Mishra, D., Kumar, J., 2019. First-principles study of the structural and electronic properties of bulk ZnS and small Zn_nS_n nanoclusters in the framework of the DFT + U method. Phys. Rev. B 100, (4) 045151.

Soltani, N., Saion, E., Hussein, M.Z., Erfani, M., Abedini, A., Bahmanrokh, G., Navasery, M., Vaziri, P., 2012. Visible light-induced degradation of methylene blue in the presence of photocatalytic ZnS and CdS nanoparticles. Int. J. Mol. Sci. 13 (10), 12242–12258.

Suhaimi, S., Shahimin, M.M., Alahmed, Z.A., Chyský, J., Reshak, A. H., 2015. Materials for enhanced dye-sensitized solar cell performance: electrochemical application. Int. J. Electrochem. Sci 10 (4), 2859–2871.

Tang, R., Su, H., Duan, S., Sun, Y., Li, L., Zhang, X., Zeng, S., Sun, D., 2015. Enhanced visible-light-driven photocatalytic performances using Bi_2WO_6/MS (M = Cd, Zn) heterostructures: facile synthesis and photocatalytic mechanisms. RSC Adv. 5 (52), 41949–41960.

Tang, J.-P., Wang, L.-L., Xiao, W.-Z., Li, X.-F., 2013. First principles study on magnetic properties in ZnS doped with palladium. Eur. Phys. J. B 86 (8), 1–5.

Wang, D.-H., Wang, L., Xu, A.-W., 2012. Room-temperature synthesis of $Zn_{0.80}Cd_{0.20}S$ solid solution with a high visible-light photocatalytic activity for hydrogen evolution. Nanoscale 4 (6), 2046–2053.

Wang, D., Guo, L., Zhen, Y., Yue, L., Xue, G., Fu, F., 2014. AgBr quantum dots decorated mesoporous Bi_2WO_6 architectures with enhanced photocatalytic activities for methylene blue. J. Mater. Chem. A 2 (30), 11716–11727.

Wang, Y., Qiao, Q.A., Cai, H., Jin, J., Gao, H., Xu, Y., 2022. Experimental and first-principles investigations on g-C_3N_4/ZnS heterostructures with enhanced photocatalyst capability. Micro & Nano Lett. 17 (11), 259–271.

Wu, L., Bi, J., Li, Z., Wang, X., Fu, X., 2008. Rapid preparation of Bi_2WO_6 photocatalyst with nanosheet morphology via microwave-assisted solvothermal synthesis. Catal. Today 131 (1–4), 15–20.

Wu, A., Jing, L., Wang, J., Qu, Y., Xie, Y., Jiang, B., Tian, C., Fu, H., 2015. ZnO-dotted porous ZnS cluster microspheres for high efficient, Pt-free photocatalytic hydrogen evolution. Scientific rep. 5 (1), 8858.

Wu, X., Hu, Y., Wang, Y., Zhou, Y., Han, Z., Jin, X., Chen, G., 2019. In-situ synthesis of Z-scheme Ag_2CO_3/Ag/AgNCO heterojunction photocatalyst with enhanced stability and photocatalytic activity. Appl. Surf. Sci. 464, 108–114.

Yagub, M.T., Sen, T.K., Afroze, S., Ang, H.M., 2014. Dye and its removal from aqueous solution by adsorption: a review. Adv. Colloid Interface Sci. 209, 172–184.

Yan, W., Xiao, Y., Yan, W., Ding, R., Wang, S., Zhao, F., 2019. The effect of bioelectrochemical systems on antibiotics removal and antibiotic resistance genes: a review. Chem. Eng. J. 358, 1421–1437.

Yu, J.C., Yu, J., Ho, W., Jiang, Z., Zhang, L., 2002. Effects of F-doping on the photocatalytic activity and microstructures of nanocrystalline TiO_2 powders. Chem. Mater. 14 (9), 3808–3816.

Zeng, W., Ren, Y., Zheng, Y., Pan, A., Zhu, T., 2021. In-situ Copper doping with ZnO/ZnS heterostructures to promote interfacial photocatalysis of microsized particles. ChemCatChem 13 (2), 564–573.

Zhang, Y.; Zhang, N.; Tang, Z.-R.; Xu, Y.-J., Graphene transforms wide band gap ZnS to a visible light photocatalyst. The new role of graphene as a macromolecular photosensitizer. *ACS nano* **2012,** *6* (11), 9777-9789.

Zhang, Z., Wang, W., Gao, E., Shang, M., Xu, J., 2011. Enhanced photocatalytic activity of Bi_2WO_6 with oxygen vacancies by zirconium doping. J. Hazard. Mater. 196, 255–262.

Zhang, J., Yu, J., Zhang, Y., Li, Q., Gong, J.R., 2011. Visible light photocatalytic H_2-production activity of CuS/ZnS porous nanosheets based on photoinduced interfacial charge transfer. Nano Lett. 11 (11), 4774–4779.

Zhang, L., Zhu, Y., 2012. A review of controllable synthesis and enhancement of performances of bismuth tungstate visible-light-driven photocatalysts. Cat. Sci. Technol. 2 (4), 694–706.

Zhao, X., Xu, Y., Wang, X., Liang, Q., Zhou, M., Xu, S., Li, Z., 2021. Construction and enhanced efficiency of Z-scheme-based ZnCdS/Bi_2WO_6 composites for visible-light-driven photocatalytic dye degradation. J. Phys. Chem. Solid 154, 110075.

Zhong, Q., Lan, H., Zhang, M., Zhu, H., Bu, M., 2020. Preparation of heterostructure g-C_3N_4/ZnO nanorods for high photocatalytic activity on different pollutants (MB, RhB, Cr (VI) and eosin). Ceram. Int. 46 (8), 12192–12199.